Article

Re–Os Pyrite Geochronological Evidence of Three Mineralization Styles within the Jinchang Gold Deposit, Yanji–Dongning Metallogenic Belt, Northeast China

Shun-Da Li [1], Zhi-Gao Wang [2], Ke-Yong Wang [1],*, Wen-Yan Cai [1], Da-Wei Peng [1], Li Xiao [3] and Jie Li [4]

[1] College of Earth Sciences, Jilin University, Changchun 130061, China; sdli16@mails.jlu.edu.cn (S.-D.L.); wenyan_1025@126.com (W.-Y.C.); pdw308zy@163.com (D.-W.P.)
[2] College of Exploration and Surveying Engineering, Changchun Institute of Technology, Changchun 130061, China; w458554302463@163.com
[3] Gold Geological Institute of CAPF, Langfang 065000, China; xiaoli1893@163.com
[4] State Key Laboratory of Isotope Geochemistry, Guangzhou Institute of Geochemistry, Chinese Academy of Sciences, Guangzhou 510640, China; jieli@gig.ac.cn
* Correspondence: wangky@jlu.edu.cn; Tel.: +86-130-6900-4095

Abstract: The Jinchang gold deposit is located in the eastern Yanji–Dongning Metallogenic Belt in Northeast China. The orebodies of the deposit are hosted within granite, diorite, and granodiorite, and are associated with gold-mineralized breccia pipes, disseminated gold in ores, and fault-controlled gold-bearing veins. Three paragenetic stages were identified: (1) early quartz–pyrite–arsenopyrite (stage 1); (2) quartz–pyrite–chalcopyrite (stage 2); and (3) late quartz–pyrite–galena–sphalerite (stage 3). Gold is hosted predominantly within pyrite. Pyrite separated from quartz–pyrite–arsenopyrite cement within the breccia-hosted ores (Py_1) yield a Re–Os isochron age of 102.9 ± 2.7 Ma (MSWD = 0.17). Pyrite crystals from the quartz–pyrite–chalcopyrite veinlets (Py_2) yield a Re–Os isochron age of 102.0 ± 3.4 Ma (MSWD = 0.2). Pyrite separated from quartz–pyrite–galena–sphalerite veins (Py_3) yield a Re–Os isochron age of 100.9 ± 3.1 Ma (MSWD = 0.019). Re–Os isotopic analyses of the three types of auriferous pyrite suggest that gold mineralization in the Jinchang Deposit occurred at 105.6–97.8 Ma (includes uncertainty). The initial $^{187}Os/^{188}Os$ values of the pyrites range between 0.04 and 0.60, suggesting that Os in the pyrite crystals was derived from both crust and mantle sources.

Keywords: Re–Os isotopes; geochronology; Jinchang gold deposit; Yanji–Dongning Metallogenic Belt

1. Introduction

Studies investigating the genesis of hydrothermal gold deposits are commonly limited by a lack of suitable minerals to directly date the age of mineralization. The age of metallogenesis is commonly inferred from the timing of magmatism, deformation, metamorphism, and alteration; however, it is still difficult to determine the age of mineralization within a deposit that records evidence for multiple tectonic and magmatic events. Accurately dating the age of mineralization is crucial in determining the genesis and prospectivity of the deposit.

Recent advances in Re–Os isotopic systematics have seen an increase in the use of this technique to directly date the age of metal deposits. These developments have included improved capability to undertake Re–Os dating of molybdenite as well as more common minerals with lower Re and Os concentrations such as pyrite and arsenopyrite [1–3]. Many studies have undertaken Re–Os geochronology work on auriferous pyrites to date the age of gold deposits [4,5].

The Jinchang Deposit is a large gold deposit located in Heilongjiang Province, Northeast China. This deposit was discovered by the Chinese Armed Police Force in the 1990s. Exploration, which continues today, has involved 96,725 m of drilling of >200 holes, and 6339 m of underground tunnel development, revealing an estimated 80.4 t gold resource with a grade of 8 g/t Au.

Previous studies of the deposit have focused on its geological features, alteration, geochemistry, fluid inclusion systematics, and geochronology [6–9]. These studies have suggested that the Jinchang Deposit is a typical magmatic–hydrothermal deposit. The interpreted age of gold mineralization in the deposit is based on the U–Pb, Rb–Sr, and Ar–Ar ages of host rocks and alteration minerals [6,10,11]. Ore formation is interpreted to have occurred between ca. 130 and 100 Ma, but the causative mechanism and timing of gold mineralization remain unclear within the context of the complex geological and magmatic evolution of the region.

We present Re–Os pyrite age data to constrain the timing of the various stages of mineralization within the Jinchang gold deposit. The results demonstrate that sulfide minerals can be used to determine the age of different types of mineralization, provide information on the origin of metals, and further our understanding of the genesis of the Jinchang gold deposit.

2. Geological Background

2.1. Geological Setting

Northeast China is located between the Siberian and North China cratons, and forms the eastern part of the Central Asian Orogenic Belt, which is the largest Phanerozoic accretionary orogen in the world [12]. Northeast China is subdivided by the Tayuan–Xiguitu, Nenjiang, and Mudanjing faults into, from east to west, the Erguna, Xinan, Songnen, and Jiamusi–Xingkai blocks (Figure 1A). The region records a prolonged geological evolution involving the emplacement of Archean–Paleoproterozoic rocks, mid–late Proterozoic rifting and subduction–collision related to the closure of the Paleo-Asian Ocean and Mesozoic subduction of the Pacific Plate and pervasive tectonomagmatic events [13,14].

The Yanji–Dongning area is located in the eastern part of Jilin and Heilongjiang provinces, within the Xingkai Block, which is bounded by the Dunhua–Mishan and Xar Moron–Changchun faults to the northwest and southeast, respectively (Figure 1B). The Yanji–Dongning area comprises Precambrian basement rocks that are overlain by Silurian–Quaternary sedimentary successions. The crystalline basement rocks were formed in high temperature and pressure environments and exposed to the surface due to the regional crustal uplift. These rocks comprise mica schists, granulites, and amphibolites. Silurian–Quaternary sedimentary successions are formed by subsequent weathering, erosion, sedimentation, and volcanic eruption. The Silurian metasedimentary rocks are overlain by Permian sandstones and greywackes, Triassic pyroclastic rocks, Jurassic intermediate–acidic pyroclastic volcanics, and Cretaceous siltstones, pelites, and tuffs. Unconsolidated Tertiary and Quaternary sediments cover the region. The main groups of faults trend NE–SW, NW–SE, and E–W. Intrusive rocks comprise Paleoproterozoic–Paleozoic granodiorites and Mesozoic granodiorites, monzogranites, and granites.

Gold mineralization occurs in the Yanji–Dongning area. The main deposits are the Nongping and Xiaoxinancha porphyry gold deposits, the mesothermal vein-hosted Naozhi Gold Deposit, and the epithermal vein-hosted Jiusangou, Wufeng–Wuxing, and Duhuangling gold deposits [15,16] (Figure 1B).
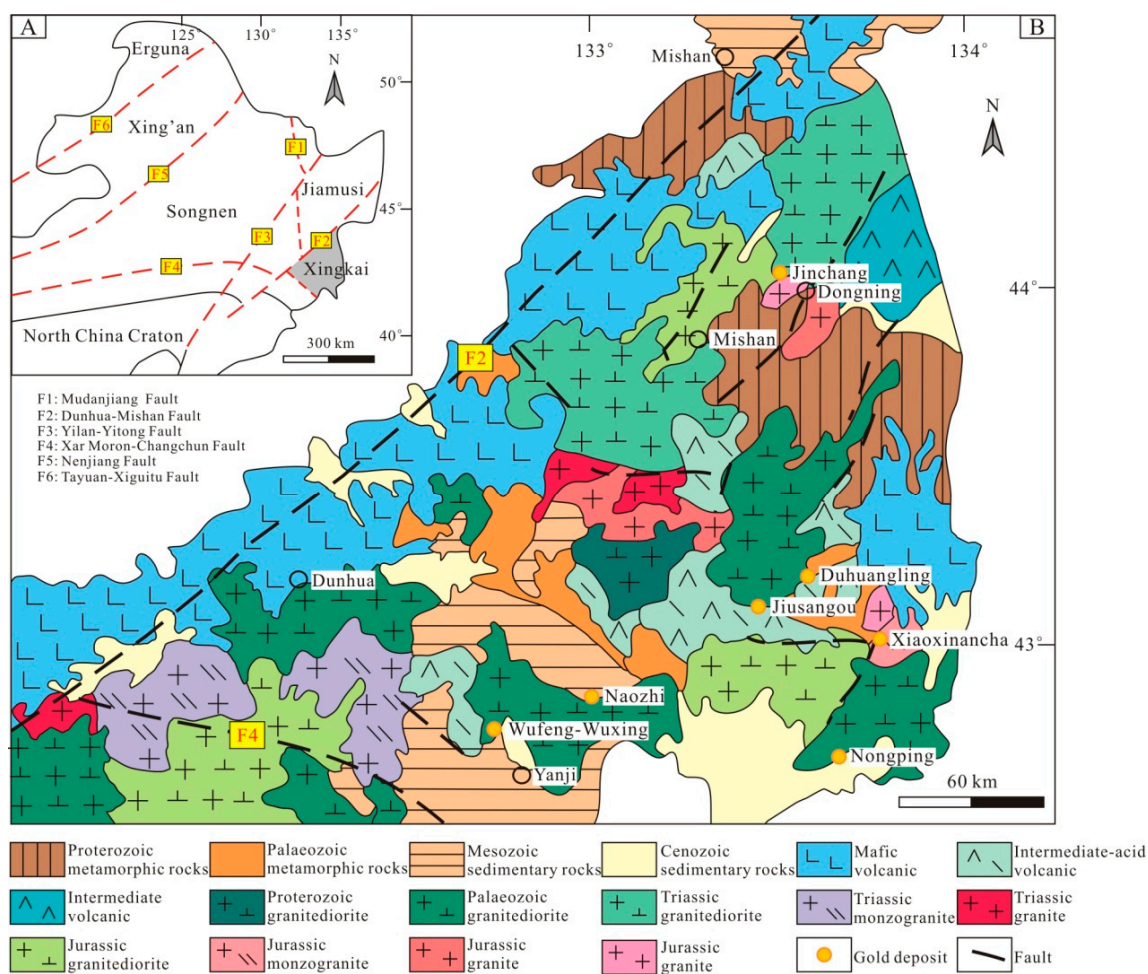
Figure 1. (**A**) Simplified tectonic map of Northeast China (modified after Wu et al. [17]). (**B**) Regional geological map of the Yanji–Dongning Metallogenic Belt, Northeast China (modified after Sun [18]), showing the location of the Jinchang gold deposit and other deposits discussed in this study.

2.2. Jinchang Gold Deposit

The Jinchang Deposit is located to the southeast of Jinchang Village (Figure 2). Outcrops are limited in this area, with exposures of andesitic–dacitic tuff restricted largely to the southeastern part of the mineralized area.

Crosscutting relationships suggest that the faults in this area can be classified into three groups with respect to the timing of mineralization. Early NE–SW, NW–SE, N–S, and E–W trending faults are widely distributed. Although they pre-date the mineralization, the intersections of these early faults facilitated fluid transport, leading to brecciation. Dome structures, and ring and radial faults in the central part of the ore field were contemporaneous with mineralization, with some orebodies occurring along these faults. Post-mineralization deformation was limited to the reactivation of early faults, which locally displaced the orebodies.
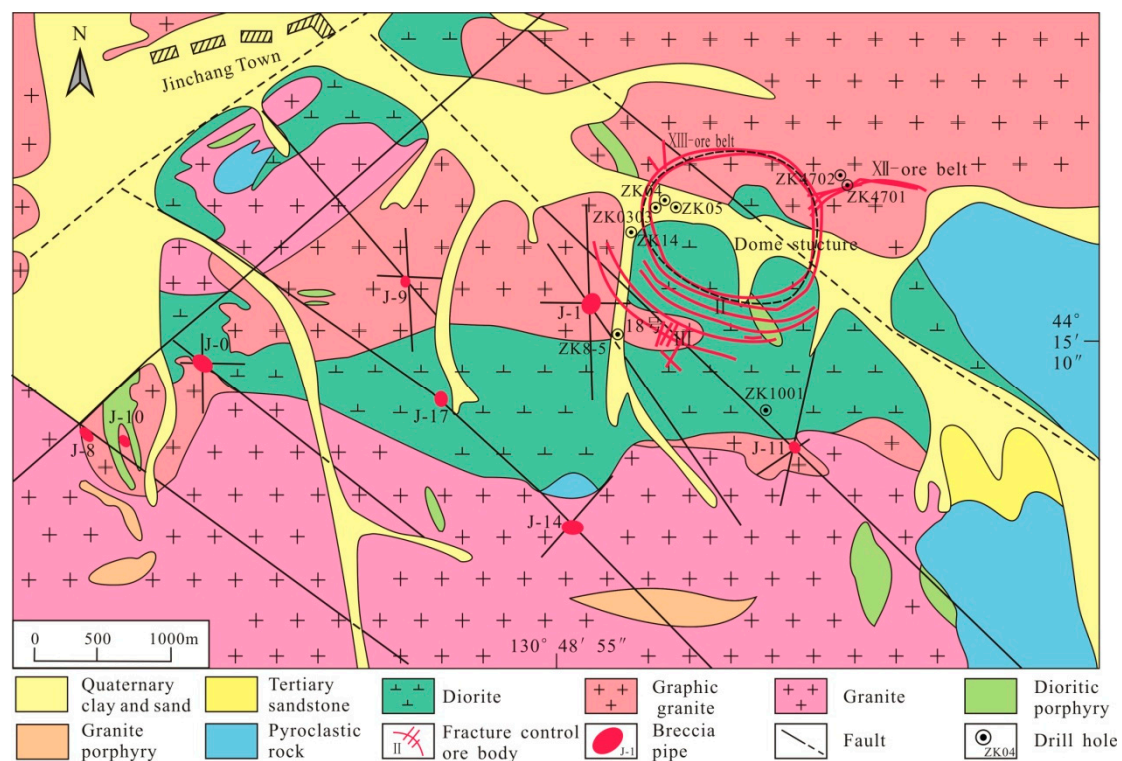
Figure 2. Geological map of the Jinchang gold deposit (modified after Zhang et al. [19]).

The variable characteristics of magmatic rocks within the ore field, their intrusive contact relationships, and age indicate a multi-stage emplacement history. The intrusive rocks comprise diorite, granite, graphic granite, granodiorite, and diorite and granite porphyries. The granitoids are calc-alkaline and high-K calc-alkaline with geochemical affinities to typical island-arc intrusive rocks [20,21]. The diorites and diorite porphyries are calc-alkaline and have geochemical affinities to adakites [20].

Diorite, graphic granite, and granite are widely exposed within the Jinchang Deposit and yield U–Pb ages of 209–185 Ma, indicating that they were emplaced after collision of the North China Craton and the Jiamusi–Xingkai Block [19,20,22,23]. These rocks are the main hosts of the ore body and are extensively altered adjacent to the mineralization. The granodiorite, diorite porphyry, and granite porphyry yield U–Pb ages of 118–106 Ma, indicating that these rocks were emplaced during subduction of the Pacific Plate beneath the Eurasian Plate [19–21,23,24]. Several diorite porphyry and granite porphyry dikes are crosscut by the ore body and are therefore interpreted to have formed prior to mineralization. Granodiorite is widespread, was emplaced in the deepest parts of the area (J11, J14, J17, and No. 18 orebodies), is extensively altered, and contains disseminated pyrite, suggesting a causal link between granodiorite emplacement and mineralization.

3. Mineralization

Exploration of the Jinchang Deposit prior to 2017 resulted in the discovery of 23 orebodies and three mineralization types (i.e., breccia pipes, disseminated veinlets, and fault-controlled veins).

3.1. Breccia Pipe Mineralization

Breccia pipe mineralization is the dominant source of gold within the deposit, accounting for >41% of the total resources in the ore field. Eight large breccia pipes are presently documented (J-0, J-1, J-8, J-9, J-10, J-11, J-14, and J-17), extending in a rough line from east to west, controlled by a major NW–SE-striking fault (Figure 2). The largest breccia pipe (J-1) is located at the intersection of N–S, NW–SE, and E–W striking faults, and occurs primarily within graphic granite. J-1 is pipe-like in form, with 5–15 m of diorite occurring above the orebody. Dikes comprising diorite porphyries

occur at a deeper structural level (Figure 3A). The orebody is 46 m long and 30 m wide at the surface, with an average thickness of 21 m and an average grade of 8.1 g/t Au. It plunges 80°–82° toward 155°–160° to a depth of 540 m. The ore rock comprises primarily cement and breccia (Figure 4A–D), the latter constituting up to 50%–80% of the total rock by volume. The breccia consists of clasts of diorite, granite, and diorite and granite porphyries that are lenticular or angular in shape and 10–25 cm in size. The breccias are cemented mainly by sulfides (i.e., pyrite, arsenopyrite, and chalcopyrite) and alteration minerals (i.e., feldspar, sericite, and quartz). Pyrite alteration is extensive in the cement, but is not observed within the breccias.
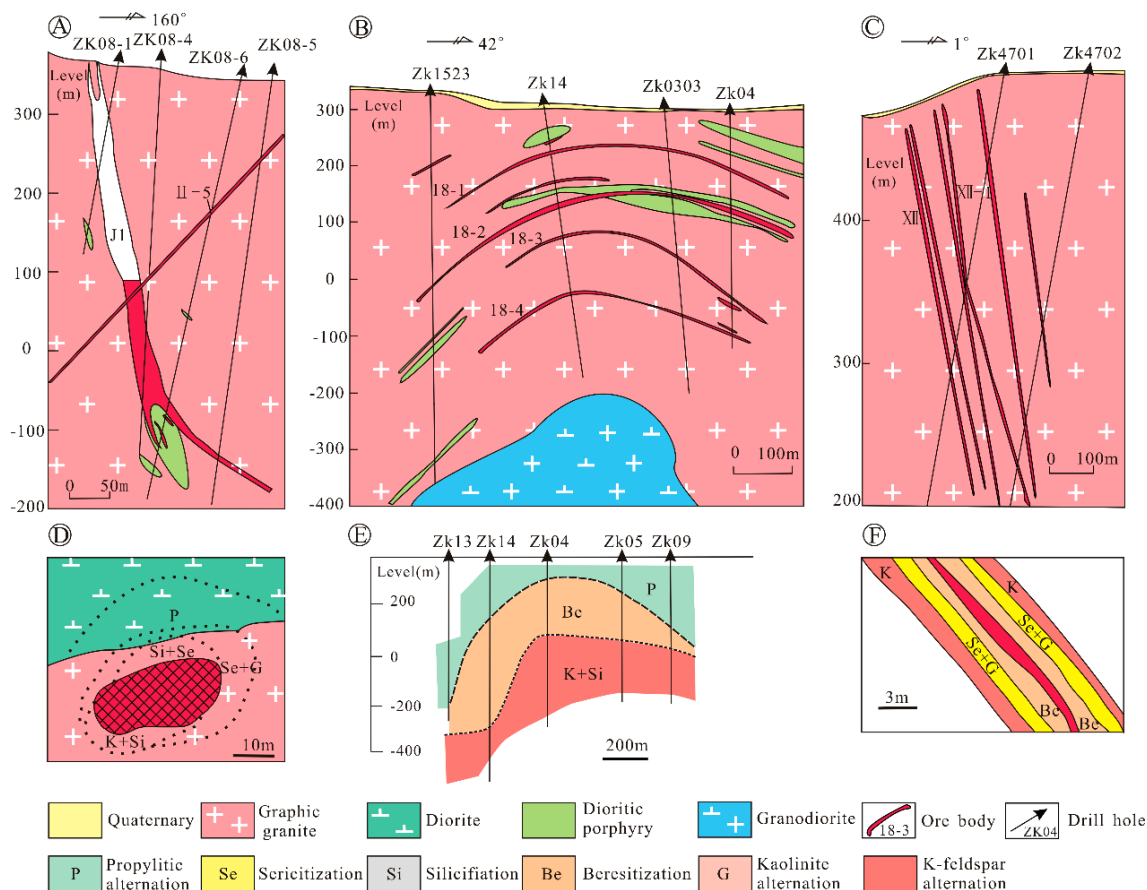

Figure 3. Geological sections and alteration patterns of the ore bodies (modified after Zhang et al. [19]); (**A**) geological cross-section of the J-1 ore body; (**B**) geological cross-section of the No. 18 ore body; (**C**) geological cross-section of the XII ore body; (**D**) alteration patterns of the J-1 ore body; (**E**) alteration patterns of the No. 18 ore body; (**F**) alteration patterns of the XII ore body.

Alteration of the wall rock is variable external to the mineralized pipe (Figure 3D). K-feldspar alteration, silicification, and sericitization are observed adjacent to the mineralized breccia pipe, whereas sericite–kaolinite and propylitic alteration occurs farther from the mineralized domain, in the outermost part of the northern breccia pipe [25].
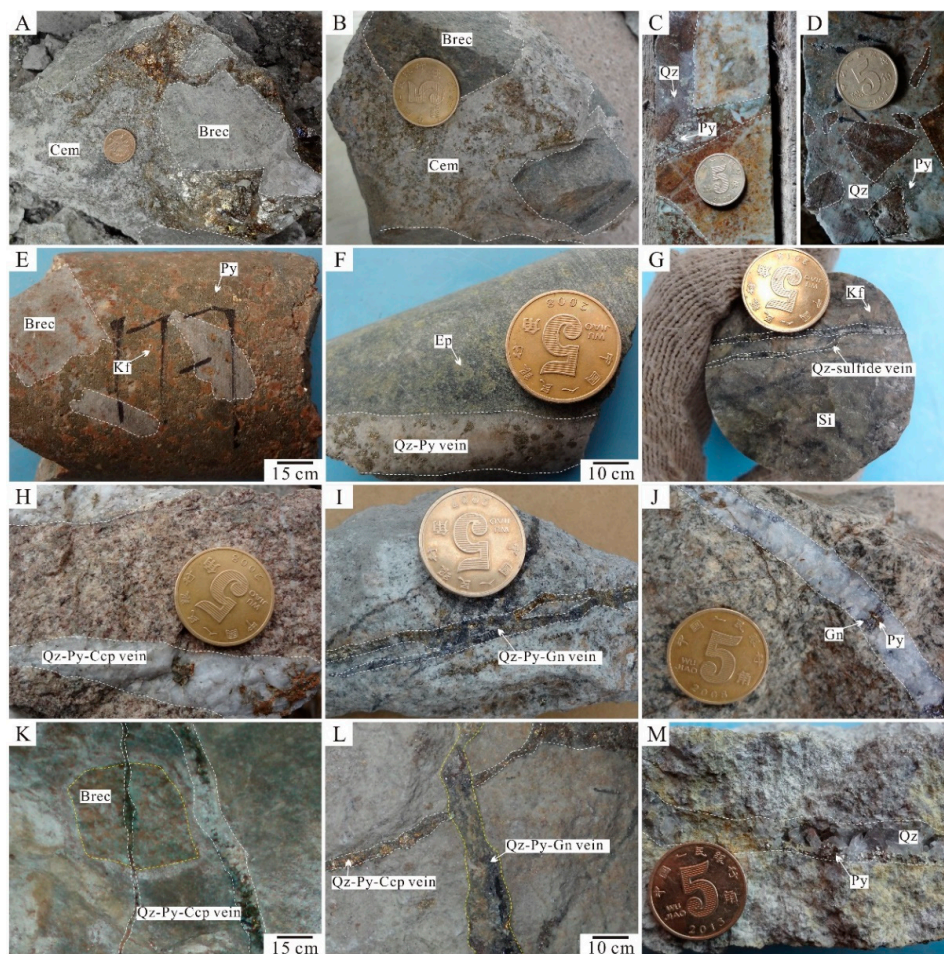
Figure 4. Photographs of ore from the Jinchang gold deposit. (**A**–**D**) Breccia-hosted ore; (**E**) K-feldspar alteration in the cement of the breccia-hosted ore; (**F**) epidote alteration of the wall-rock surrounding a quartz–pyrite vein; (**G**) silicification of the wall-rock surrounding a quartz–sulfide veinlet; (**H**) quartz–pyrite–chalcopyrite vein; (**I**,**J**) quartz–pyrite–galena veins; (**K**) breccia-hosted ore crosscut by a quartz–pyrite–chalcopyrite vein; (**L**) quartz–pyrite–chalcopyrite vein crosscut by a quartz–pyrite–galena vein; (**M**) drusy structure in the ore. Abbreviations: Cem, cement; Brec, breccia; Qz, quartz; Ep, epidote; Kf, K-feldspar; Si, silicification; Py, pyrite; Ccp, chalcopyrite; Gn, galena; Sp, sphalerite.

3.2. Veinlet Disseminated Mineralization

The No. 18 orebody is a typical example of veinlet disseminated mineralization, accounting for ~20% of the total resources in the ore field. The orebody is hosted within graphic granite and several diorite porphyry dikes beneath a dome structure. The orebody appears to be layered and is divided into four sub-bodies that are labeled 18-1 to 18-4, from top to bottom (Figure 3B). These sub-bodies are 0.6–7.9 m thick, ~800 m long, and have an average grade of 11.23 g/t Au. They strike toward 138°, dip ~47° to the SW, and extend to depths of 160–490 m. Drill holes have intersected granodiorite at depth. The ore minerals are mainly pyrite and chalcopyrite, and lesser molybdenite, chalcocite, bornite, azurite, sphalerite, galena, and gold. Quartz is the main gangue mineral, with minor sericite, chlorite, and epidote.

The wall rock and concealed granodiorite observed in the drill holes are both altered. From depth to the surface, the alteration varies from K-feldspar alteration and silicification to beresitization and finally propylitic alteration [25] (Figure 3D).

3.3. Fault-Controlled Vein Mineralization

Fault-controlled vein mineralization accounts for 39% of the total Au resources in the ore field, including within ore belts II, III, and XII. Vein development was controlled primarily by ring and radial

faults associated with a dome. The forming of the dome is resulted from intrusion of magma. Ore belt XII is typical of this type of mineralization, as it comprises a swarm of veins within graphic granite that are controlled by E–W-trending radial faults in the northeastern part of the lava dome (Figure 2). This ore belt is 460 m long, 0.2–1.78 m thick, and has an average grade of 9.34 g/t Au. The orebodies plunge 70°–80° toward 001°–005° and extend to depths of 190–510 m. The ore minerals include pyrite, sphalerite, galena, and minor chalcopyrite. The gangue minerals are predominantly quartz and minor carbonate (Figure 4H).

Wall rock alteration occurs over several meters from the fault-controlled veins, is symmetrical about the veins, and is more extensive than alteration associated with the other mineralization styles (Figure 3F). With increasing distance from the ore body, the wall rock is affected by quartz–sericite, sericite–kaolinite, and subsequently K-feldspar alteration, although the boundaries between these domains are gradational [25].

The Jinchang Deposit comprises a number of hydrothermal veins and mineral assemblages. The mineral assemblages and their crosscutting relationships indicate three mineralization stages (Figures 4–6). Stage 1 mineralization occurred primarily within the cement of the breccia-hosted ore. This was the most important ore-forming stage as it involved the deposition of abundant native gold (Figure 5A). Stage 1 mineralization is also characterized by milky white quartz, pyrite, and lesser arsenopyrite, K-feldspar, and sericite (Figure 4A–D). Pyrite is the most abundant ore mineral, commonly occurring within the cement as coarse-grained pentagonal dodecahedra and tetragonal trisoctahedra crystals (Figure 4A,B), and locally as fine- to medium-grained aggregates (Figure 4C).
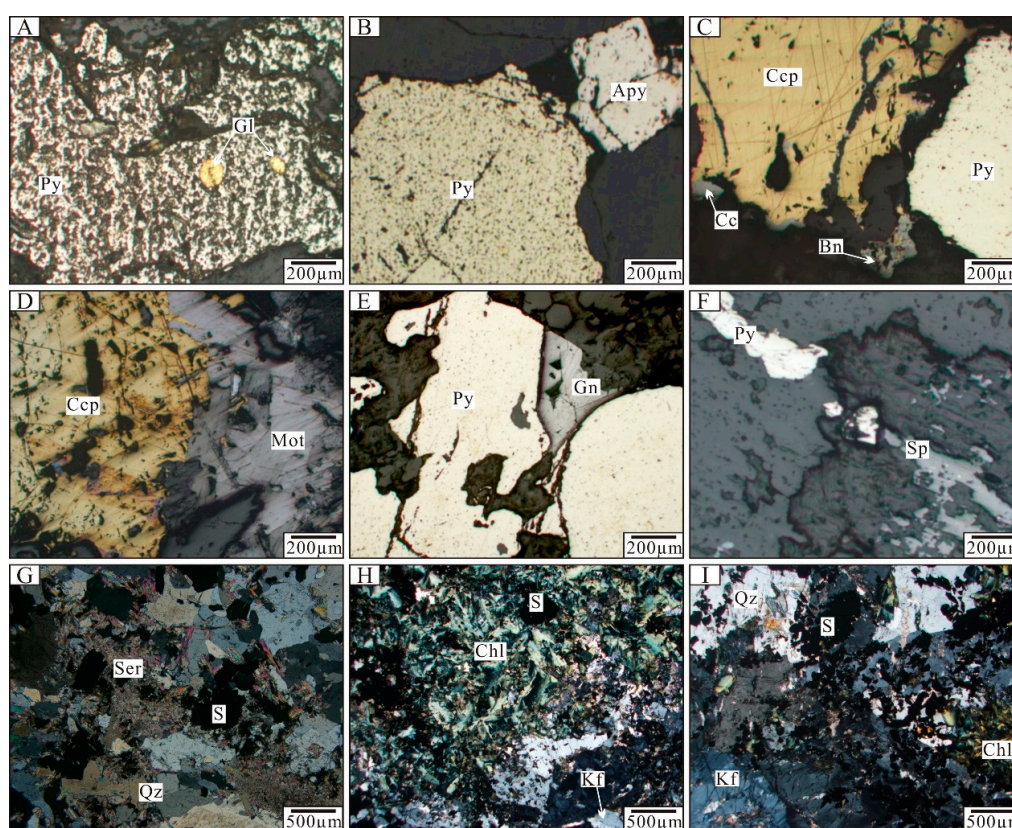

Figure 5. Photomicrographs of key mineral assemblages in the Jinchang Deposit. (**A**) Native gold in pyrite; (**B**) coexisting pyrite and arsenopyrite; (**C**) pyrite–chalcopyrite–chalcocite–bornite assemblage; (**D**) chalcopyrite–molybdenite assemblage; (**E**) coexisting pyrite and galena; (**F**) pyrite–sphalerite veinlet; (**G**) beresitization of the wall-rock; (**H**,**I**) chloritization and K-feldspar alteration of wall-rock. Abbreviations: Qz, quartz; Ser, sericite; Chl, chlorite; Kf, K-feldspar; S, sulfide; Py, pyrite; Ccp, chalcopyrite; Gn, galena; Sp, sphalerite; Apy, arsenopyrite; Mot, molybdenite; Bn, bornite; Cc, chalcocite.

Figure 6. Mineral paragenesis for the Jinchang gold deposit.

Stage 2 mineralization involved the formation of economic quartz–pyrite–chalcopyrite veins and widespread in veinlet disseminated ores (Figure 4H). These veins also comprise small amounts of molybdenite, chalcocite, bornite, azurite, gold, chlorite, and epidote. Chalcopyrite is the dominant sulfide and occurs as anhedral crystals intergrown with pyrite in quartz veins (Figure 5C). Molybdenite is rare, typically exhibits a hexagonal shape, and occurs as aggregates that are intergrown with chalcopyrite (Figure 5D). The breccia-hosted ore is crosscut by the quartz–pyrite–chalcopyrite veins and is observed in the tunnel at the 30 m level (Figure 4K).

Stage 3 mineralization involved the formation of quartz–pyrite–galena–sphalerite veins (Figure 4I,J) that also contain minor gold, chlorite, epidote, kaolinite, and calcite. Pyrite commonly occurs as hypidiomorphic or xenomorphic crystals that are intergrown with galena and sphalerite in quartz veinlets (Figure 5E,F). These veins have a limited distribution and commonly cut across quartz–pyrite–chalcopyrite veins, suggesting that they formed relatively late (Figure 4L). These veins are associated with fault-controlled vein mineralization and are not observed in the breccia.

4. Sample Selection and Analytical Methods

Fifteen samples of auriferous pyrite were collected from five drill holes (ZKE01, ZK05, ZK11, ZK14, and ZK4702) and underground tunnels for Re–Os analysis (Table 1). Re–Os isotopic analyses were undertaken on pyrites from the cement of breccia-hosted ore (Py_1), within quartz–pyrite–chalcopyrite veins (Py_2), and within quartz–pyrite–galena–sphalerite veins (Py_3). These three types of pyrite are representative of the observed breccia pipe, veinlet disseminated, and fault-controlled vein mineralization styles, respectively. Samples that displayed late-stage sulfide replacement were not analyzed to avoid the influence of late-stage hydrothermal alteration on the results.

We employed the Carius tube digestion technique commonly used in our lab for Re–Os chemistry [26]. About 0.5–2 g of each powdered sample was digested and equilibrated with ^{185}Re- and ^{190}Os-enriched spikes in reverse aqua regia (7.5 mL concentrated HNO_3 + 2.5 mL concentrated HCl) for 24 h at 240 °C in sealed Carius tubes. Osmium was extracted by solvent extraction into CCl_4 and back-extraction into concentrated HBr [27,28], with subsequent cleanup by microdistillation [29]. The Re fraction was separated and purified using anion column chromatography.

Mass spectrometry procedures for the Os are given in Li et al. [30]. Os was loaded onto Pt filaments and measured as OsO_3^- ions by negative-thermal ionization mass spectrometry (N-TIMS) using the electron multiplier mode on a Thermo-Finnigan Triton [31,32] at the State Key Laboratory of Isotope Geochemistry, Guangzhou Institute of Geochemistry, Chinese Academy of Sciences, Guangzhou, China. Repeated analyses of the Os standard solution (Merck Chemical AA standard solution) yield a mean $^{187}Os/^{188}Os$ value of 0.12052 ± 0.00032 (2 SD, n = 5) for the period of analysis. These values are in good agreement with a value of 0.12022 ± 0.00020 (2 SD, n = 14) measured on the same mass spectrometer in Faraday cup mode [33].

Table 1. Re–Os isotopic data for auriferous pyrites from various locations in the Jinchang gold deposit.

Pyrite	Sample	Location	Re Conc (ppt)	2SE	Os Conc (ppt)	2SE	$^{187}Os/^{188}Os$	2σ	$^{187}Re/^{188}Os$	2SE	Initial $^{187}Os/^{188}Os$
Py_1	J1-1	ZKE01 at 84 m level	9906	268.75	11.50	0.21	70.72	0.79	42,853	1408.28	−2.80
	J1-2	ZKE01 at 64 m level	9643	147.37	11.78	0.21	52.22	0.47	31,501	740.43	−1.82
	J1-3	30 m level middle section	10,475	159.15	14.61	0.36	16.48	0.40	10,855	314.64	−2.14
	J1-4	30 m level middle section	9908	104.95	11.82	0.37	68.68	0.93	41,376	1354.88	−2.31
	J1-5	30 m level middle section	9856	121.56	11.66	0.24	58.53	0.71	35,295	1024.55	−2.02
Py_2	J18-1	ZK05 at 280 m level	4194	76.99	5.09	0.09	50.28	0.38	31,074	804.77	−2.57
	J18-2	ZK05 at 362 m level	4087	61.62	6.12	0.05	19.04	0.16	11,203	196.09	−0.01
	J18-3	ZK11 at 235 m level	4224	153.08	6.20	0.05	21.30	0.17	12,395	460.54	0.22
	J18-4	ZK11 at 342 m level	4541	96.97	5.95	0.05	36.70	0.23	21,496	498.65	0.14
	J18-5	ZK14 at 166 m level	4125	73.58	5.55	0.05	52.36	0.43	30,856	706.91	−0.12
Py_3	Jh-1	374 m level middle section	1437	26.20	3.12	0.05	7.36	0.10	4054	96.79	0.54
	Jh-2	374 m level middle section	1255	36.95	2.94	0.02	7.19	0.08	3957	119.94	0.53
	Jh-3	374 m level middle section	1346	20.85	3.57	0.02	6.47	0.05	3527	56.64	0.53
	Jh-4	ZK4702 at 186 m level	1735	13.05	3.21	0.03	11.39	0.13	6443	76.36	0.55
	Jh-5	ZK4702 at 287 m level	1185	20.46	3.02	0.02	11.21	0.06	6354	83.55	0.52

Rhenium mass fraction was analyzed by inductively coupled plasma mass spectrometry (Thermo Elemental X2 Series). A conventional low volume quartz impact bead spray chamber with a Peltier cooled (3 °C) and a 0.4 mL·min^{-1} borosilicate nebulizer (MicroMist GE) was used in the determinations. Ion lens settings, nebulizer gas flow rate and torch position were optimized daily using a 10 ng·mL^{-1} tuning In–Ce mixture standard solution in order to obtain the high instrumental sensitivity and low oxide production levels. A peristaltic pump was not used, as free aspiration of the nebulizer provided better signal stability. The details of measurements are described elsewhere [34].

Total procedural blanks (TPBs) were 0.72 ± 0.44 pg (1SE, *n* = 2) with an ^{187}Os/^{188}Os ratio of 0.67 ± 0.55 (1SE, *n* = 2) on average for Os and 4.0 ± 0.1 pg (1SE, *n* = 2) for Re. All data were corrected for the procedural blank for each analytical batch. Blank contributions for mafic-ultrmafic rock samples were generally insignificant. The average values (^{187}Os/^{188}Os = 0.13369 ± 0.00014, Os = 0.340 ± 0.032 ppb, Re = 0.691 ± 0.002 ppb, 1SE, *n* = 2) are in good agreement with published data for basaltic reference material BIR-1 [35–37].

Errors for Re and Os concentration and ^{187}Re/^{188}Os and ^{187}Os/^{188}Os isotopic ratios were determined by numerical error propagation and include spike calibration uncertainties an in-run precision during mass-spectrometry measurements for both Re and Os.

5. Results

The blank-corrected Re and Os data for 15 pyrite samples from the Jinchang Deposit are provided in Table 1. Isochrons for these samples were calculated using ISOPLOT software [38] and employing a ^{187}Re decay constant of 1.666×10^{-11} year^{-1} [39].

Total Re and Os concentrations in Py$_1$ range between 9643 and 10,475, and 11.50 and 14.61 ppt, respectively, corresponding to ^{187}Re/^{188}Os ratios between 10,855 and 42,853, and ^{187}Os/^{188}Os ratios of 16.48–70.72. Py$_1$ yielded an individual model 3 Re–Os isochron age of 102.9 ± 2.7 Ma (2SE (Standard error); mean square weighted deviation (MSWD) = 0.17; initial ^{187}Os/^{188}Os (I$_{Os}$) = −2.1 ± 1.0; Figure 7A).
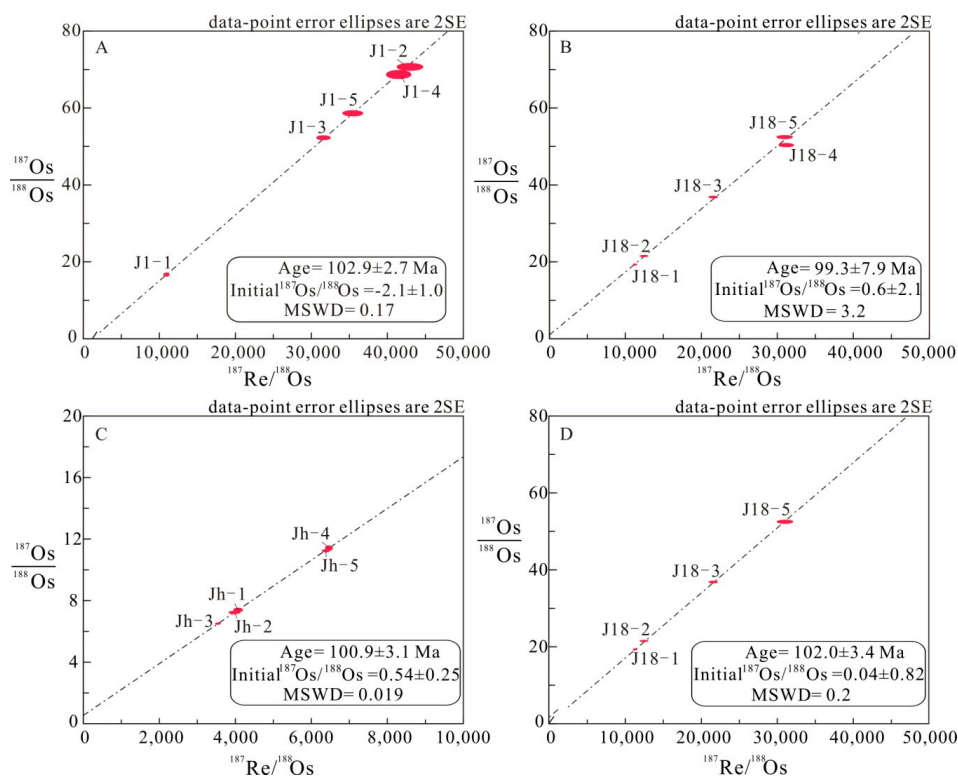

Figure 7. Re–Os isochron plots of stage 1–3 pyrites from the Jinchang Gold Deposit. (**A**) Isochron age of five analyses of Py$_1$; (**B**) isochron age of five analyses of Py$_2$; (**C**) isochron age of five analyses of Py$_3$; (**D**) isochron age of four analyses (excluding J18-4) of Py$_2$.

Rhenium (Re) and Osmium (Os) concentrations in Py_2 range between 4087 and 4541, and 5.09 and 6.20 ppt, respectively. The $^{187}Re/^{188}Os$ and $^{187}Os/^{188}Os$ ratios of Py_2 range between 11,203 and 31,074, and 19.04 and 52.36, respectively. Five samples yielded an isochron age of 99.3 ± 7.9 Ma (MSWD = 3.2) and I_{Os} of 0.6 ± 2.1; however, the MSWD is indicative of a relatively large degree of scatter in the data. The results indicate a 0.02 probability of the data fitting the criteria for a model 3 isochron calculated using the ISOPLOT software (Figure 7B), which may be a result of Os loss. Excluding sample J18-4 from the calculation yielded a more precise individual model 3 Re–Os isochron age of 102.0 ± 3.4 Ma (2SE; MSWD = 0.2; I_{Os} = 0.04 ± 0.82; Figure 7D).

The Py_3 crystals yielded Re and Os concentrations of 1185–1735 and 2.94–3.20 ppt, respectively, corresponding to $^{187}Re/^{188}Os$ ratios of 3957–6443 and $^{187}Os/^{188}Os$ ratios of 6.47–11.39. Py_3 yielded an individual model 3 Re–Os isochron age of 100.9 ± 3.1 Ma (2SE; MSWD = 0.019; I_{Os} = 0.54 ± 0.25; Figure 7C).

6. Discussion

6.1. Timing of Metallogenesis

To establish the ore genesis of the Jinchang Deposit, it is necessary to obtain precise geochronological data. Previous geochronological studies established that the Jinchang gold deposit formed during the Cretaceous (Table 2). $^{40}Ar/^{39}Ar$ geochronology of quartz from quartz–pyrite veins in orebody J-1 yielded an age of 122.53 ± 0.88 Ma [10] and an $^{40}Ar/^{39}Ar$ plateau age of 122 Ma [6]. Quartz from quartz–pyrite veins in orebody XII yielded an $^{40}Ar/^{39}Ar$ isochron age of 119 ± 5 Ma [11]. Sphalerite from orebody J-9 yielded an $^{40}Ar/^{39}Ar$ isochron age of 129 ± 0.8 Ma [11]. The specific age of mineralization, however, remains unclear. This is firstly due to the fact that quartz and sphalerite are not Au-bearing minerals within the Jinchang Deposit, so the analyses of these minerals define the age of alteration rather than gold mineralization. Secondly, the Jinchang Deposit records evidence of multiple phases of hydrothermal activity, adding further complexity. Even monomineralic quartz samples may contain inclusions of K-feldspar and sericite which, due to their relatively high K concentrations, may influence the $^{40}Ar/^{39}Ar$ results. The relatively low precision of the $^{40}Ar/^{39}Ar$ fast neutron activation method means that a spread of ages may be observed between the actual ages of different hydrothermal events, further limiting our ability to constrain the nature of the evolving system [40].

The Re–Os radiogenic system in pyrite can be used as a high-precision geochronometer. This dating method has the advantage of an isotopic closure temperature of >500 °C, meaning that the results are not easily disturbed by subsequent metamorphism or deformation and therefore are likely to record the timing of primary crystallization [26,41–43]. Since pyrite is the dominant host of gold in the Jinchang Deposit, the age of pyrite formation will likely record the age of gold mineralization.

Five Re–Os isotopic analyses of pyrite reported by Zhang et al. [44] yielded an isochron age of 114 ± 22 Ma; however, the uncertainty on the age is large, probably owing to two factors. First, it is unclear which of the mineralization stages the analyzed pyrite relates to. Pyrite from different ore veins and mineralization stages were analyzed together, resulting in a low degree of confidence in the isochron age and a large age uncertainty [45]. Second, impure separates may yield Re–Os mixed ages of both the pyrite and other material, rather than solely the age of the pyrite [26].

In the present study, three types of pyrite (Py_1, Py_2, and Py_3), reflecting three styles of mineralization, were analyzed. Each stage yields sufficient representative pyrite samples to enable a robust interpretation of the age data. Py_1, Py_2, and Py_3 yield similar metallogenic ages that are sequentially younger from Py_1 to Py_3, indicating that the ages are representative and accurate.

Sericite from altered granite in drill holes ZK14 and ZK04 in the No. 18 orebody yields a Rb–Sr age of 107 ± 5 Ma. Together, the sericite and pyrite yield a Rb–Sr age of 104 ± 6 Ma [19]. This alteration is considered to reflect the initial stage of mineralization in the deposit. The age of gold mineralization should therefore be slightly younger than these ages. The age of gold mineralization is consistent with the Re–Os pyrite age (105.6–97.8 Ma) obtained in this study. A sample of granodiorite was collected

from a depth of 380 m in drill hole ZK1001 and yielded a $^{206}Pb/^{238}U$ age of 106.8 ± 2.0 Ma [21], which is broadly similar to the age of ore formation. Crystallization of a large intrusion and the main stage of mineralization in the development of a gold deposit may occur over several million years [46]. Similarities in the timing of granodiorite emplacement and mineralization within the Jinchang Deposit suggest that the former is the likely source and driver of the latter. The occurrence of granodiorite at depth suggests that mineralization may also extend to deeper structural levels.

Table 2. Isotopic ages of rocks and minerals from the Jinchang gold deposit.

Test object	Method	Age	Reference
Diorite	U–Pb	209 ± 1.4 Ma	[23]
Granite	U–Pb	203.62 ± 0.86 Ma	[20]
Granite	U–Pb	202.1 ± 3.0 Ma	[22]
Granite	U–Pb	201 ± 3 Ma	[19]
Granite	U–Pb	184.69 ± 0.98 Ma	[20]
Dioritic porphyrite	U–Pb	118.4 ± 1.6 Ma	[9]
Dioritic porphyrite	U–Pb	116 ± 2 Ma	[23]
Dioritic porphyrite	U–Pb	115.7 ± 2.0 Ma	[9]
Dioritic porphyrite	U–Pb	111.5 ± 1.2	[22]
Granite porphyry	U–Pb	113.5 ± 3.6 Ma	[24]
Granite porphyry	U–Pb	112.62 ± 0.85 Ma	[23]
Granite porphyry	U–Pb	110 ± 3 Ma	[19]
Granodiorite	U–Pb	106.8 ± 2.0 Ma	[21]
Quartz–pyrite veins in the J-1 orebody	$^{40}Ar/^{39}Ar$	122.53 ± 0.88 Ma	[10]
Quartz–pyrite veins in the J-2 orebody	$^{40}Ar/^{39}Ar$ plateau	122 Ma	[6]
Quartz from quartz–pyrite veins of orebody XII	$^{40}Ar/^{39}Ar$	119 ± 5 Ma	[11]
Sericite from altered granite	Rb–Sr	107 ± 5 Ma	[19]
Sericite and pyrite from altered granite	Rb–Sr	104 ± 6 Ma	[19]
Sphalerite from J-9 orebody	$^{40}Ar/^{39}Ar$	129 ± 0.8 Ma	[11]
Pyrite from J1 orebody	Re–Os	114 ± 22 Ma	[44]
Py_1	Re–Os	102.9 ± 2.7 Ma	This study
Py_2	Re–Os	102.0 ± 3.4 Ma	This study
Py_3	Re–Os	100.9 ± 3.1 Ma	This study

6.2. Re–Os Isotopic Compositions and Implications for the Ore Source

In addition to constraining the age of ore formation, the Re–Os isotopic system can be used to identify the source of the ore-forming material [3,26]. Excluding negative values that are inferred to be erroneous or indicative of systematic disturbance, the I_{Os} values derived from Re–Os pyrite isochrons in this study range from 0.04 to 0.60 (Figure 7). The I_{Os} values calculated for individual samples range from 0.14 to 0.54 (Table 1), assuming that Py_1, Py_2, and Py_3 formed at 102.9, 102.0, and 100.9 Ma, respectively In both instances, the I_{Os} values are lower than the upper crustal $^{187}Os/^{188}Os$ average value of 1.9256 [47]. The I_{Os} values lie between the $^{187}Os/^{188}Os$ values of chondrite (0.1263), which is representative of the mantle composition at 102 Ma, and those of the lower crust (0.64–0.96) [48]. These observations suggest that the ore-forming materials in this deposit were derived from a mixed crust–mantle source. In the Re–Os versus common Os diagram (Figure 8; after Lambert et al. [1]), the compositions of the auriferous pyrites are approximately consistent with those of mantle melts and the lower crust, suggesting that the ore-forming materials were derived from a mixed crust–mantle source, with the largest contribution being from the lower crust.
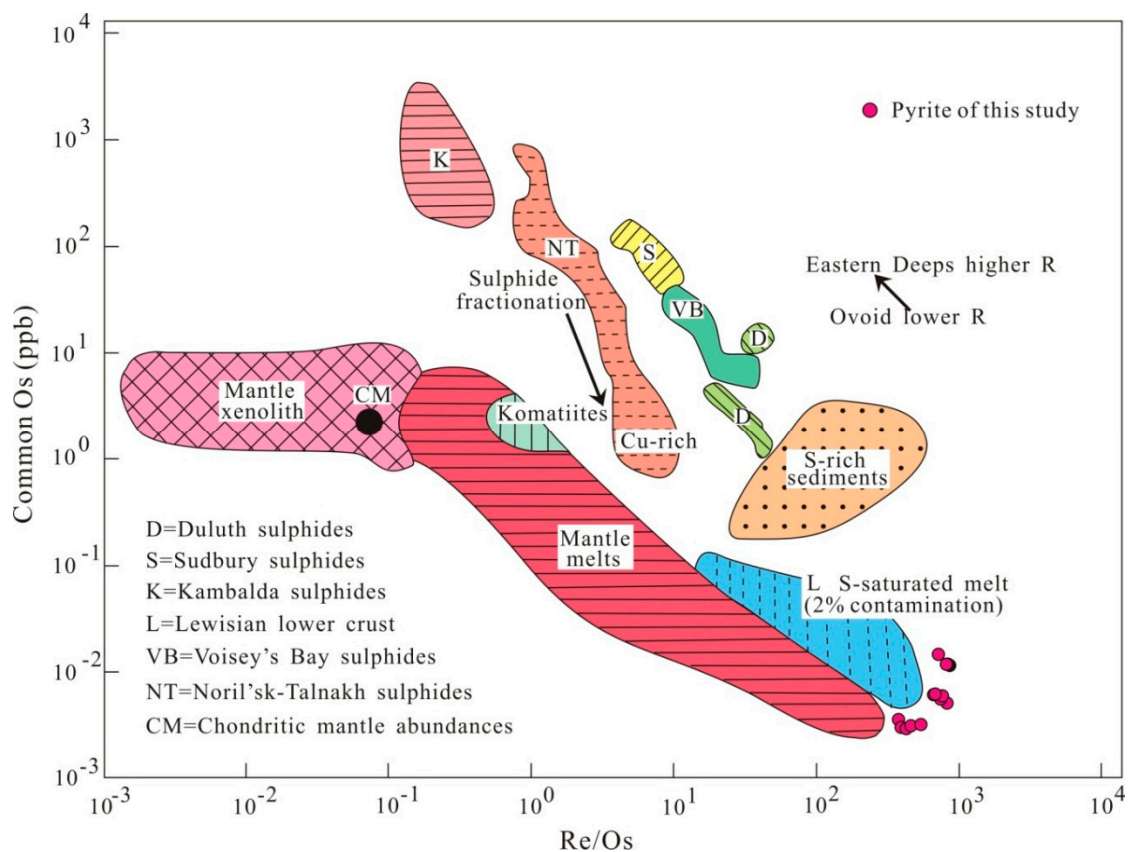
Figure 8. Re/Os versus common Os diagram for auriferous pyrite from the Jinchang Deposit (modified after Lambert et al. [1]).

6.3. Genesis and Metallogenic Setting of the Jinchang Deposit

The study area records evidence for collision, deformation, and extension associated with subduction of the west Pacific Plate during the late and early stages of the Indosinian and Yanshannian orogenies, respectively [15]. During the early stages of collision (210–190 Ma), I-type granites intruded the Yanji–Dongning area as a result of upper crustal melting [13,16,49]. At ca. 140 Ma, the tectonic setting changed from compression to extension due to closure of the Pacific Ocean during continent–continent collision [50]. During the Early Cretaceous (130–100 Ma), northeast China was undergoing extension, as indicated by bimodal volcanic rocks in the Xiaoxing'anling–Zhangguangcailing region [51–53] and the widespread development of metamorphic core complexes in the Songliao Basin [54].

The timing of mineralization in the various ore deposits within the Yanbian–Dongning area has been investigated by Ar–Ar, Rb–Sr, Re–Os, and U–Pb geochronology of quartz and muscovite, sericite, sulfides, and zircon, respectively [18,40,54–56]. These analyses yielded ages between 126 and 95 Ma, indicating that an important mineralization event took place at this time in the Yanbian–Dongning area. Previous studies have suggested that the ore deposits formed due to regional-scale lithospheric thinning [13,15,16,57].

In the Jinchang Deposit, granodiorite is extensively altered and mineralized, and yields a U–Pb age of 106.8 ± 2.0 Ma (MSWD = 0.65, n = 20) [21]. Re–Os dating of pyrites from the ore body yields ages of 105.6–97.8 Ma (This study), which are interpreted as the timing of ore formation. The ages of diagenesis and metallogenesis are within error of each other, suggesting that mineralization was related to granodiorite emplacement. Upwelling mantle-derived magmas would have provided heat to partially melt the lower crust as well as fluids that extracted metals from the lower crust and facilitated their migration to shallower levels (i.e., toward the upper crust). The Re–Os isotopic analyses of pyrites in this study, and the S and Pb isotopic compositions of ores analyzed previously, also suggest that

the ore-forming components were derived from both crust and mantle sources [19]. The ore-forming fluids are interpreted to have contained abundant volatiles that migrated to the intersections of faults. When the fluid pressure exceeded the pressure of the overlying rocks, cryptoexplosions and thereby breccia pipe mineralization occurred. Vein-disseminated mineralization occurred adjacent to the intrusive body, within the surrounding rock. Magma intrusion caused ring and radial faults to form around the magma dome, creating space for hydrothermal migration, fluid mixing, metal precipitation, and thus fault-controlled vein mineralization.

7. Conclusions

1. Re–Os isotopic analyses of auriferous pyrites from the Jinchang Deposit yielded ages of 102.9–100.9 Ma, which are interpreted to reflect the age of gold mineralization.
2. Re–Os isotopic compositions suggest that the ore-forming material was derived from lower crustal and mantle sources.
3. Three types of mineralization were contemporaneous, but occurred at different structural locations. Granodiorite emplacement is considered the most likely cause of mineralization.

References

1. Lambert, D.D.; Foster, J.G.; Frick, L.R. Re-Os isotopic systematics of the Voisey's Bay Ni-Cu-Co magmatic ore system, Labrador, Canada. *Lithos* **1999**, *47*, 69–88. [CrossRef]
2. Mao, J.W.; Du, A.D. The 982 Ma Re-Os age of copper-cickel sulfide ores in the Baotan area, Guangxi, and its geological significance. *Sci. China Ser. D* **2001**, *31*, 992–998. (In Chinese)
3. Stein, H.J.; Morgan, J.W.; Schersten, A. Re-Os dating of low-level highly radiogenic (LLHR) sulfides: The Harnas gold deposit, southwest Sweden, records continental-scale tectonic events. *Econ. Geol.* **2000**, *95*, 1657–1671. [CrossRef]
4. Mathur, R.; Ruiz, J.; Titley, S.; Gibbins, S.; Margotomo, W. Different crustal sources for Au-rich and Au-poor ores of the grasberg Cu–Au porphyry deposit. *Earth Planet. Sci. Lett.* **2000**, *183*, 7–14. [CrossRef]
5. Kirk, J.D.; Ruiz, J.; Kesler, S.E.; Simon, A.; Muntean, J.L. Re-Os age of the pueblo Viejo epithermal deposit, Dominican Republic. *Econ. Geol.* **2014**, *109*, 503–512. [CrossRef]
6. Jia, G.Z.; Chen, J.R.; Yang, Z.G.; Bian, H.Y.; Wang, Y.Z.; Liang, H.J.; Jin, T.H.; Li, Z.H. Geology and genesis of the superlarge Jinchang gold deposit. *Acta Geol. Sin.* **2005**, *79*, 661–670. (In Chinese)
7. Zhang, D.H.; Wang, Y.; Wang, D.; Xu, W.X.; Wang, Y.Z.; Zhang, W.Z. Geochemistry of ore forming fluids and genesis of gold ore bodies in the dome-shaped magmatic body-hosted Jinchang gold deposit, Heilongjiang province. *Min. Depos.* **2006**, *25*, 155–158. (In Chinese)
8. Wang, Y.; Xi, B.B.; Zhang, D.H.; Zhang, W.H. Geochemical characteristics of fluid inclusions in Jinchang gold deposit, Heilongjiang Province. *Min. Depos.* **2007**, *26*, 184–194. (In Chinese)
9. Zhao, Y.S.; Yang, L.Q.; Chen, Y.F.; Qing, M.; Yan, J.P.; Ge, L.S. Geochemisry and zircon U-Pb geochronology of the diorite porphyry associated with the Jinchang Cu-Au deposit, Heilongjiang Province. *Acta Petrol. Sin.* **2012**, *28*, 451–467. (In Chinese)
10. Chen, J.R.; Jin, B.Y.; Wang, K.Q.; Wu, Y.H. Research Report on Metallogenic Regulation and Prognosis of Jinchang Gold Deposit, Dongning Country, Heilongjiang Province. 2007. Available online: http://ww

w.wanfangdata.com.cn/details/detail.do?_type=conference&id=6314107 (accessed on 22 August 2007). (In Chinese)

11. Qing, M.; Tang, M.G.; Xiao, L.; Zhao, Y.S.; Han, X.J. Automatic Laser Probe ^{40}Ar/^{39}Ar isochron ages of the quatrz and sphalerite from the Jinchang gold deposit, Dongning County, Heilongjiang Province, and their prospecting implications. *Geol. Prospect.* **2012**, *48*, 991–999. (In Chinese)

12. Xiao, W.J.; Santosh, M. The western Central Asian Orogenic Belt: A window to accretionary orogenesis and continental growth. *Gondwana Res.* **2014**, *25*, 1429–1444. [CrossRef]

13. Mao, J.W.; Xie, G.Q.; Zhang, Z.H.; Li, X.F.; Wang, Y.T.; Zhang, C.Q.; Li, Y.F. Mesozoic large-scale metallogenic pulses in North China and corresponding geodynamic settings. *Acta Petrol. Sin.* **2005**, *21*, 169–188.

14. Xu, W.L.; Wang, F.; Meng, E.; Gao, F.H.; Pei, F.P.; Yu, J.J.; Tang, J. Paleozoic-Early Mesozoic Tectonic Evolution in the Eastern Heilongjiang Province NEChina: Evidence from Igneous Rock Association U-Pb Geochronlolgy of Detrital Zircons. *J. Jilin Univ. (Earth Sci. Ed.)* **2012**, *5*, 1378–1389. (In Chinese)

15. Sun, J.G.; Chen, L.; Zhao, J.K.; Men, L.J.; Feng, W.; Chen, D.; Liang, S.N. SHRIMP U-Pb dating of zircons from Late Yanshanian granitic complex in Xiaoxinancha gold-rich copper orefield of Yanbian and its geological implications. *Miner. Depos.* **2008**, *3*, 319–328. (In Chinese)

16. Ren, Y.S.; Chen, C.; Zou, X.T.; Zhao, H.L.; Hao, Y.J.; Hou, H.N.; Hu, Z.C.; Jiang, G.H. The age, geological setting, and types of gold deposits in the Yanbian and adjacent areas, NE China. *Ore Geol. Rev.* **2016**, *73*, 284–297. [CrossRef]

17. Wu, F.Y.; Sun, D.Y.; Ge, W.C.; Zhang, Y.B.; Grant, M.L.; Wilde, S.A.; Jahn, B.M. Geochronology of the Phanerozoic granitoids in northeastern China. *J. Asian Earth Sci.* **2011**, *41*, 1–30. [CrossRef]

18. Sun, J.G.; Zhang, Y.; Xing, S.W.; Zhao, K.Q.; Zhang, Z.J.; Bai, L.A.; Ma, Y.B.; Liu, Y.S. Genetic types, ore-forming age and geodynamic setting of endogenic molybdenum deposits in the eastern edge of Xing-Meng orogenic belt. *Acta Petrol. Sin.* **2012**, *28*, 1317–1332. (In Chinese)

19. Zhang, H.F.; Li, S.R.; Santosh, M.; Liu, J.J.; Diwu, C.R.; Zhang, H. Magmatism and metallogeny associated with mantle upwelling: Zircon U–Pb and Lu–Hf constraints from the gold-mineralized Jinchang granite, NE China. *Ore Geol. Rev.* **2013**, *54*, 138–156. [CrossRef]

20. Han, S.J.; Yang, Y.C.; Ye, S.Q.; Khomich, V.G.; Boriskina, N.G.; Wang, X.Y. U–Pb zircon and geochemical constraints on age and genesis of granitoids from the Jinchang Au deposit in Heilongjiang, NE China. *Geol. J.* **2017**. [CrossRef]

21. Wang, Z.G. Mineralization and Metallogenic Prediction of Jinchang Cu-Au Deposit in Dongning, Heilongjiang Province. Ph.D. Thesis, Jilin University, Changchun, China, 2018. (In Chinese)

22. Lu, Y.H.; Zhang, Y.; Lai, Y.; Wang, Y.Z. LA–ICP-MS zircon U–Pb dating of magmatism and mineralization in the Jinchang gold ore-field, Heilongjiang province. *Acta Petrol. Sin.* **2009**, *25*, 2902–2912. (In Chinese)

23. Zhao, Y.S. Porphyry Gold System of the Jinchang Camp in the Yanbian-Dongning Metallogenic Belt, NE China. Ph.D. Thesis, China University of Geosciences, Beijing, China, 2013. (In Chinese)

24. Qian, Y.; Sun, F.Y.; Li, B.L.; Chen, J.; Diwu, C.R. Geochemistry and U–Pb geochrony of zircon from granite porphyry of Jinchang gold deposit in Heilongjiang, China and its geological significance. *J. Chengdu Univ. Technol.* **2012**, *39*, 362–371. (In Chinese)

25. Chen, J.R.; Li, H.G.; Jin, B.Y.; Wu, Y.H.; Wang, Y.Z.; Yu, W.Q. Geological features and the deep metallogenic forecast of the No. J-1 gold body in the Jinchang gold deposit, Heilongjiang. *Gold Geol.* **2002**, *8*, 8–12. (In Chinese)

26. Shirey, S.B.; Walker, R.J. Carius tube digestion for low-blank rhenium-osmium analysis. *Anal. Chem.* **1995**, *67*, 2136–2141. [CrossRef]

27. Cohen, A.S.; Waters, F.G. Separation of osmium from geological materials by solvent extraction for analysis by thermal ionization mass spectrometry. *Anal. Chim. Acta* **1996**, *332*, 269–275. [CrossRef]

28. Pearson, D.G.; Woodland, S.J. Solvent extraction/anion exchange separation and determination of PGE (Os, Ir, Pt, Pd, Ru) and Re-Os isotopes in geological samples by isotope dilution ICP-MS. *Chem. Geol.* **2000**, *165*, 57–107. [CrossRef]

29. Roy-Barman, M. Mesure du Rapport ^{187}Os/^{186}Os dans les Basaltes et les Péridotites: Contribution à la Systématique ^{187}Re-^{187}Os dans le Manteau. Ph.D. Thesis, Université de Paris VII, Paris, France, 1993.

30. Li, J.; Zhao, P.P.; Liu, J.G.; Wang, X.C.; Yang, Y.; Wang, G.Q.; Xu, J.F. Reassessment of Hydrofluoric Acid Desilicification in the Carius Tube Digestion Technique for Re-Os Isotopic Determination in Geological Samples. *Geostand. Geoanal. Res.* **2015**, *39*, 17–30. [CrossRef]

31. Creaser, R.A.; Papanastassiou, D.A.; Wasserburg, G.J. Negative thermal ion mass spectrometry of osmium, rhenium and iridium. *Geochim. Cosmochim. Acta* **1991**, *55*, 397–401. [CrossRef]

32. Volkening, J.; Walczyk, T.; Heumann, K.G. Osmium isotope ratio determinations by negative thermal ionization mass spectrometry. *Int. J. Mass Spectrom. Ion Process.* **1991**, *105*, 147–159. [CrossRef]

33. Li, J.; Liang, X.R.; Xu, J.F.; Suzuki, K.; Dong, Y.H. Simplified technique for the measurements of Re-Os isotope by multicollector inductively coupled plasma mass spectrometry (MC-ICP-MS). *Geochem. J.* **2010**, *44*, 73–80. [CrossRef]

34. Li, J.; Jiang, X.Y.; Xu, J.F.; Zhong, L.F.; Wang, X.C.; Wang, G.Q.; Zhao, P.P. Determination of Platinum-Group Elements and Re-Os Isotopes using ID-ICP-MS and N-TIMS from a Single Digestion after Two-Stage Column Separation. *Geostand. Geoanal. Res.* **2014**, *38*, 37–50. [CrossRef]

35. Ishikawa, A.; Senda, R.; Suzuki, K.; Dale, C.W.; Meisel, T. Re-evaluating digestion methods for highly siderophile element and ^{187}Os isotope analysis: Evidence from geological reference materials. *Chem. Geol.* **2014**, *384*, 27–46. [CrossRef]

36. Li, J.; Wang, X.C.; Xu, J.F.; Xu, Y.G.; Tang, G.J.; Wang, Q. Disequilibrium-induced initial Os isotopic heterogeneity in gram aliquots of single basaltic rock powders: Implications for dating and source tracing. *Chem. Geol.* **2015**, *406*, 10–17. [CrossRef]

37. Zhang, J.; Li, J.; Long, X.P.; Sun, S.L.; Yin, L.; Dai, M.N. Rhenium–osmium isotope measurements of geological reference material BIR–1a: Evaluation of homogeneity and implications for method validation and quality control. *Geostand. Geoanal. Res.* **2017**. [CrossRef]

38. Ludwig, K. *Isoplot/Ex Version 2.0: A Geochronological Toolkit for Microsoft Excel*; Special Publication 1a; Geochronology Center: Berkeley, CA, USA, 1999.

39. Smoliar, M.L.; Walker, R.J.; Morgan, J.W. Re–Os ages of group IA, IIA, IVA and IVB iron meteorites. *Science* **1996**, *271*, 1099–1102. [CrossRef]

40. Men, L.J. An Ore-forming Fluid Study on Late Mesozoic Epithermal Au–Cu Deposits in Yanbian–Dongning Area: Implication for the Metallogenic Mechanism. Ph.D. Thesis, Jilin University, Changchun, China, 2011. (In Chinese)

41. Stein, H.J.; Sundblad, K.; Markey, R.J.; Morgan, J.W.; Motuza, G. Re-Os ages for Archean molybdenite and pyrite, Kuittila-Kivisuo, Finland and Proterozoic molybdenite, Kabeliai, Lithuania: Testing the chronometer in a metamorphic and metasomatic setting. *Min. Depos.* **1998**, *33*, 329–345. [CrossRef]

42. Brenan, J.M.; Cherniak, D.J.; Rose, L.A. Diffusion of osmium in pyrrhotite pyrite: Implications for closure of the Re-Os isotopic system. *Earth Plant. Sci. Lett.* **2000**, *180*, 399–413. [CrossRef]

43. Nozaki, T.; Kato, Y.; Suzuki, K. Re-Os geochronology of the Iimori Besshi-type massive sulfide deposit in the Sanbagawa metamorphic belt, Japan. *Geochim. Cosmochim. Acta* **2010**, *74*, 4322–4331. [CrossRef]

44. Zhang, P.; Huang, X.W.; Cui, B.; Wang, B.C.; Yin, Y.F.; Wang, J.R. Re-Os isotopic and trace element compositions of pyrite and origin of the Cretaceous Jinchang porphyry Cu-Au deposit, Heilongjiang Province, NE China. *J. Asian Earth Sci.* **2016**, *129*, 67–80. [CrossRef]

45. Huang, X.W.; Qi, L.; Wang, Y.C.; Liu, Y.Y. Re-Os dating of magnetite from the Shaquanzi Fe-Cu deposit, Eastern Tianshan, NW China. *Sci. China Ser. D* **2014**, *57*, 267–277. [CrossRef]

46. Wei, J.H.; Liu, C.Q.; Zhao, Y.X.; Li, Z.D. Time Span of the Major Ore-forming Stages of the Wulong Gold Deposit, Liaoning. *Geol. Rev.* **2001**, *47*, 433–437. (In Chinese)

47. Esser, B.K.; Turekian, K.K. The osmium isotopic composition of the continental crust. *Geochim. Cosmochim. Acta* **1993**, *57*, 3093–3104. [CrossRef]

48. Saal, A.E.; Rudnick, R.L.; Ravizza, G.E.; Hart, S.R. Re-Os isotope evidence for the composition, formation and age of the lower continental crust. *Nature* **1998**, *393*, 58–61. [CrossRef]

49. Han, S.J.; Sun, J.G.; Bai, L.A.; Xing, S.W.; Chai, P.; Zhang, Y.; Yang, F.; Men, L.J.; Li, Y.X. Geology and ages of porphyry and medium- to high-sulphidation epithermal gold deposits of the continental margin of northeast China. *Int. Geol. Rev.* **2013**, *55*, 287–310. [CrossRef]

50. Qi, J.P.; Chen, Y.J.; Franco, P. Geological characteristics and tectonic setting of the epithermal deposits in the Northeast China. *J. Miner. Petrol.* **2005**, *25*, 47–59. (In Chinese)

51. Ge, W.C.; Lin, Q.; Sun, D.Y.; Wu, F.Y.; Won, C.K.; Lee, M.W.; Jin, M.S.; Yun, S.H. Geochemical characteristics of the Mesozoic basalts in Da Hinggan Ling: Evidence of the mantle-crust interaction. *Acta Petrol. Sin.* **1999**, *15*, 397–407. (In Chinese)

52. Zhang, W.H.; Qin, J.Y.; Zhang, D.H.; Tian, L.; Wang, L.L.; Wang, Y. Fluid inclusion indicators in prophyry Au deposits: Taking Jinchang gold deposit, Heilongjiang Province as an example. *Acta Petrol. Sin.* **2008**, *24*, 2011–2016. (In Chinese) [CrossRef]

53. Xu, W.L.; Pei, F.P.; Wang, F.; Meng, E.; Ji, W.Q.; Yang, D.B.; Wang, W. Spatial-temporal relationships of Mesozoic volcanic rocks in NE China: Constraints on tectonic overprinting and transformations between multiple tectonic systems. *J. Asian Earth Sci.* **2013**, *74*, 167–193. [CrossRef]

54. Zhao, Y.J.; Sun, J.G.; Wang, Q.H.; Men, L.J.; Li, Y.X.; Guo, J. ^{40}Ar/^{39}Ar laser probe dating and discussion on metallogenic epoch of epithermal Au-Cu deposit in Yanbian area of Jilin. *Earth Sci. Front.* **2010**, *17*, 156–169. (In Chinese)

55. Li, Z.Z.; Li, S.R.; Zhang, H.F. Wall rock alteration and metallogenic chronology of Jinchang gold deposit in Dongning County, Heilongjiang Province. *Min. Depos.* **2009**, *01*, 83–92. (In Chinese)

56. Ren, Y.S.; Ju, N.; Zhao, H.L.; Wang, H.; Hou, K.J.; Liu, S. Geochronology and geochemistry of metallogenetic porphyry bodies from the Nongping Au-Cu deposit in the eastern Yanbian area, NE China: Implications for metallogenic environment. *Acta Geol. Sin. (Engl. Ed.)* **2012**, *86*, 619–629.

57. Mao, J.W.; Wang, Z.L. A preliminary study on time limits and geodynamic setting of large-scale metallogeny in East China. *Min. Depos.* **2000**, *19*, 289–296. (In Chinese)